Surface & Coatings Technology 538 (2026) 133868

Contents lists available at ScienceDirect

Surface & Coatings Technology

journal homepage: www.elsevier.com/locate/surfcoat

Interfacial modification and adhesion improvement of Mo—C and W—C nanolayers by ion irradiation

A.S. Racz [a,*], M. Nemeth [a], O. Krafcsik [a,b], U. Kentsch [c], M. Panjan [d], M. Göken [e], M. Wurmshuber [e], Z. Fogarassy [a]

[a] HUN-REN Centre for Energy Research, Konkoly Thege M. út 29-33, 1121, Budapest, Hungary
[b] Department of Atomic Physics, Institute of Physics, Budapest University of Technology and Economics, Műegyetem rakpart 3., H-1111, Budapest, Hungary
[c] Helmholtz-Zentrum Dresden-Rossendorf, Bautzner Landstraße 400, 01328, Dresden, Germany
[d] Jožef Stefan Institute, Jamova 39, 1000, Ljubljana, Slovenia
[e] Department of Materials Science & Engineering, Friedrich-Alexander-Universität Erlangen-Nürnberg, Germany

ARTICLE INFO

Keywords:
Carbide
Ion irradiation
Nano-layer
Ramped load scratch
Nanoindenter

ABSTRACT

The adhesion of coatings to substrates is a critical requirement in a wide range of applications, including catalysis and protective coatings. Ion irradiation can improve coating adhesion through ion mixing at the coating–substrate interface. Herein, carbide-rich nanolayers were produced by irradiating C/Mo and C/W multilayer systems deposited on silicon with Xe ions (40–120 keV, 0.25–0.5 $\times$ 10^{16} ions/cm^2). XPS depth profiling confirmed the formation of carbide-rich regions at the interface. Coating adhesion was evaluated by ramped-load scratch testing using a nanoindenter. Depending on the irradiation conditions, the critical load for delamination increased from 18.2 to 45.1 mN for the C/W multilayer and from 27.2 to approximately 36.9 mN for the C/Mo multilayer. Cross-sectional transmission electron microscopy was used to examine the structural changes along selected regions of the scratch tracks. Clear differences were observed between irradiated and non-irradiated coatings: while non-irradiated coatings exhibited interfacial delamination and substrate cracking, irradiated coatings showed buckling with reduced crack propagation, indicating improved coating–substrate adhesion. The larger adhesion improvement of the C/W multilayer is attributed to more pronounced irradiation-induced interfacial mixing and substrate amorphization. The results demonstrate that ion irradiation effectively modifies the coating–substrate interface and enhances the adhesion of carbide-rich nanolayers.

*Corresponding author.

1. Introduction

Good adhesion between coatings and substrates is a critical requirement in a wide range of applications, including catalysis, energy-generation systems, and protective coatings. [1,2] Multilayer systems can offer an efficient way of controlling residual stress, improve adhesion and enhance toughness of coated systems. [3] To address this issue, several techniques have been developed to evaluate the adhesion between a coating and its substrate, although each method has its own limitations. Basic tests, such as the Scotch tape method, provide only qualitative information. More advanced methods have been developed to quantify adhesion strength, with the scratch test being one of the most widely used comparative techniques. In this test, a diamond indenter is drawn across the coating surface under progressively increasing load until the coating fails in a consistent manner. The load at which this failure occurs is referred to as the 'critical load' and serves as an indicator of adhesion strength. Failure can be identified in several ways, such as the initiation of cracks around the indenter, delamination or spalling of the coating, or the formation of a track where the coating has been completely removed. [4] In the case of physical vapor deposition (PVD) the adhesion of the coating can be critical due to the remaining residual stresses in the film, while in the case of CVD the application of hazardous gases and elevated temperatures might be disadvantageous for certain applications [5,6]. E.g.: the adhesion of PVD coatings on stainless steel can be inadequate because of the substrate's surface properties. Achieving strong adhesion requires several key factors: ensuring an atomically clean surface through pre-deposition sputtering, carefully selecting the deposition temperature to promote interfacial

* Corresponding author.
E-mail address: racz.adel@ek.hun-ren.hu (A.S. Racz).

https://doi.org/10.1016/j.surfcoat.2026.133868
Received 16 June 2026; Received in revised form 28 July 2026; Accepted 21 August 2026
Available online 22 August 2026

diffusion, and tailoring the coating structure to avoid tensile residual stresses near the interface. [7] To fully benefit from functional coatings, a strong bond between the coating and the substrate is essential. Adhesion strength is known to depend on the coating–substrate contact area which is influenced by the surface roughness. Numerous studies suggest that a rougher interface can enhance adhesion by increasing the area available for mechanical interlocking. However, in the case of certain thin coatings, such as those produced by physical vapor deposition, better adhesion may be achieved on smoother surfaces with very low roughness, as this can reduce stress concentrations and limit crack initiation and propagation. Therefore, the optimal surface roughness should be carefully selected based on the specific coating type and deposition process to achieve the best adhesion performance. [8]

Ion beam irradiation represents a versatile approach in the modification and formation of coatings. Being a non-equilibrium process, ion irradiation can induce significant changes in materials, including defect generation, atomic intermixing across the interface, compound formation, and even the emergence of metastable phases. While some of these effects may be detrimental under certain conditions, they can also be harnessed in a controlled manner to produce beneficial modifications, especially at the coating–substrate interface. In the context of adhesion, ion beam techniques offer a unique advantage by enabling tailored interface engineering without the need for high-temperature processing. The induced intermixing at the interface can effectively increase the bonding between the coating and the substrate, while defect formation may enhance mechanical interlocking on a microscopic scale. Additionally, ion irradiation can influence residual stress states and microstructural features, both of which play a role in adhesion performance. Experimental studies support these effects. E.g. sputtered TiN coatings on stainless steel were irradiated with MeV Ag ions and the coatings were studied before and after irradiation. Automatic scratch tester (Revetest) equipped with acoustic emission (AE) was applied, the microstructural changes were investigated by scanning electron microscope. It was shown a shift from spallation to buckling failure modes in scratch tests, indicating stronger interfacial bonding and increased compressive stress. [9] The adhesion properties of DLC coating on stainless steel substrate have been improved by carbon and carbon/silicon implantation respectively. The adhesion properties were investigated by tensile pull-off tests while the microstructural changes due to ion irradiation were evaluated by STEM. [10] Ion irradiation-based methods have been also used for improving the adhesion of polymers to metal. E.g.: Poly(ethylene naphthalate) (PEN) films were irradiated with 150 keV Xe^+ ions at fluences varying from 1×10^{14} to 1×10^{16} ions/cm^2, the adhesion was tested by ramped load scratch test in a nanoindenter. [11] It is important to note that in none of the above studies were extensive cross-sectional electron microscopy (XTEM) investigations carried out along the different stages of the scratch tracks. To the best of our knowledge, systematic XTEM investigations performed along different regions of scratch tracks remain scarce, despite their importance for understanding coating failure mechanisms.

Transition-metal carbides have several advantageous properties, such as high hardness, wear resistance, corrosion resistance [12] and some of them - molybdenum and tungsten carbide - show catalytic activity, as well. [2,13,14] We have shown recently that it is possible to produce tungsten carbide rich nano-layers by irradiating C/W multilayer systems (individual layer thicknesses 10–20 nm) on a Si substrate with noble gases, the coatings exhibited excellent corrosion and scratch resistance. [15,16] However, the adhesion properties of these irradiation-modified layers have not yet been investigated. Following these studies, the present work extends the investigation to C/Mo multilayer systems as an additional carbide-forming model material. We have also previously shown that the extent of irradiation-induced mixing can be estimated using TRIDYN simulations. [17] In the present study xenon irradiations are investigated as this noble gas ion with higher mass enables efficient mixing within the near-surface region at moderate ion energies while limiting the modification depth. The average atomic number of C/Mo and C/W systems is vastly different – 24 and 40 resp. - which may influence irradiation-induced mixing behaviour and structural evolution. The main aim of the study is to investigate how ion irradiation conditions influence the adhesion properties of carbide-based multilayer systems and to correlate the observed adhesion behaviour with irradiation-induced microstructural changes. Single-crystal Si was employed as a model substrate owing to its well-defined microstructure, smooth surface and suitability for cross-sectional TEM investigations, allowing irradiation-induced structural changes at the coating–substrate interface to be analysed with high spatial resolution.

Herein, we investigate the adhesion of Mo- and W-carbide-rich nanolayers formed by xenon irradiation of C/Mo and C/W multilayers deposited on single-crystal Si. The ramped load scratch test performed in nanoindenter has shown differences in the critical load of coating delamination for the differently irradiated samples. Extensive transmission electron microscopy measurements have been performed for investigating the different structural changes during the different scratching phases. The observed deformation and failure behaviour was interpreted based on XTEM observations together with XPS depth profiling and SRIM simulations. The combined results provide insight into the roles of irradiation-induced interfacial mixing and substrate amorphization in the adhesion improvement. It was shown that ion irradiation produces a thin amorphous Si layer beneath the coating, while scratching induces further amorphization at low loads followed by recrystallization at higher loads. In the irradiated samples, no substrate cracking was observed during scratching and the coating buckled instead of undergoing abrupt delamination, whereas substrate cracks were found in the non-irradiated samples, indicating an enhancement of the mechanical integrity of the coating–substrate system.

2. Experimental section

2.1. Production of carbide-rich nanolayer by means of ion beam mixing (IBM)

The carbide-rich nano-layers were produced by means of ion mixing of different C/W and C/Mo multilayer structures.

The initial multilayer structures were made on Si single crystal by sputter deposition of pure C and W/Mo layers; the detailed description of the procedure is given in Ref. [18]. Its essence is the following. The sputtering was made in a Balzers Sputron sputtering chamber. To avoid mixing due to plasma, the sample was far from the plasma, thus during the layer growth the temperature was always below 100 °C. The thickness of the sputtered layer was controlled by quartz-crystal microbalance. The following structures have been made for this study: C (9 nm) / W (23 nm) / C (9 nm) // Si substrate and C (12 nm) /Mo (18 nm) /C (12 nm) /Si substrate; for easier reference these samples will be called as 102010-W and 102010-Mo. For the ion mixing we applied xenon ions (40–120 keV, fluence 2.5–5 $\times$ 10^{15} Xe^+/cm$^{2)}$ at room temperature (Model B8385 implanter). SRIM simulation [19] was applied to choose the ion irradiation parameters. This Monte Carlo-based simulation approach was employed to estimate the ion penetration depth (projected range), energy deposition profile and defect production during irradiation. The main aim was to select irradiation conditions where the ions reached all relevant interfaces within the multilayer structure. 80 keV Xe ions were applied for the C/Mo system and 120 keV Xe ions for the C/W system. In addition, a 40 keV Xe irradiation was performed on the C/W system as a reference condition. At this energy, the projected range (~13 nm) remained within the coating and did not reach the coating–substrate interface, allowing the role of coating–substrate interface modification in adhesion improvement to be distinguished from the effects of irradiation confined to the coating.

2.2. XPS studies

The composition of the non-irradiated and irradiated samples has been investigated by X-ray photoelectron spectroscopy (XPS) depth profiling with 500 eV monoatomic argon sputtering (50° respect to the surface normal). The investigations were performed in a Thermo Fisher Scientific Escalab Xi^+ instrument (anode Al K-alpha). The size of the X-ray spot was 650 μm, no charge neutralizer was used. Tungsten (4f), molybdenum silicon (2p), carbon (1 s) and oxygen (1 s) high-resolution spectra were measured within the spectral range of interest (ca. 20 eV around the core level emission peaks) at 20 eV pass energies with 0.1 eV steps and 50 ms dwell time per data point. All spectra were collected at normal emission angle. The amount of material producing the measured XPS spectrum is generally determined from the area of the XPS peak [20]. CasaXPS software [21] was applied to determine this area from the high resolution spectra by applying background subtraction. The carbon spectra were decomposed to components by various line shapes, Lorentzian Asymmetric Lineshape (LA) [22] was used for the graphitic components while Gaussian-Lorentzian functions (mixing parameter of 30) were used for the carbide and C—O components. Peak positions and peak widths (FWHM) of the components were carefully constrained to construct a reliable peak model which was valid throughout the depth profile. Due to the strong overlap, the Mo 3d and W 4f peaks cannot be resolved into individual components such as metallic molybdenum and molybdenum carbide. For the elemental composition calculations, the commonly used infinitely thick homogeneous sample model was applied. This model assumes a uniform elemental distribution within the XPS information depth. Since the thickness of the individual layers is comparable to the information depth of the emitted photoelectrons, this approximation does not fully describe the actual multilayer structure. Therefore, the calculated compositions should be considered as approximate values, providing a comparative estimation of the irradiation-induced compositional changes rather than absolute concentrations. Linear or Shirley-type baseline was used to define the peak areas. In case of C 1 s quantification, the overlapping Mo 3d loss peak was also considered when the C concentration was low, and Mo concentration was high. The ratio of the elements was calculated from the integral intensities of the XPS lines, using sensitivity factors given by the manufacturer. The carbide formation could be well followed by the shape change of the carbon peak. As an example, the decomposed C (1 s) XP spectra of the 102010-Mo 80 keV, 5×10^{15} Xe^+ irradiated sample is provided in Fig. 1. The spectrum from a transition region where graphitic and carbide components are present together is shown in Fig. 1a while the main carbide region is depicted in Fig. 1b.

2.3. Scratch test

Although the total coating thicknesses were approximately 40 nm, the scratch test was employed as a comparative method to evaluate coating adhesion. Since all coatings had comparable thicknesses and were deposited on the same Si substrate, differences in the measured critical loads are primarily associated with ion-irradiation-induced modifications of the coating–substrate interface. Similar nanoscratch approaches have previously been successfully applied to ultrathin coatings. For example, Beake et al. investigated tetrahedral amorphous carbon films with thicknesses of 5, 20 and 80 nm deposited on Si(100) using nanoscratch, nanoindentation and fretting experiments to evaluate their tribological and mechanical performance. Despite the differences in contact pressure and failure mechanisms, a clear correlation between the fretting and nanoscratch tests was found. [23] In the present study the scratch tests were performed in a KLA Nano Indenter® G200 with a spheroconical diamond tip of 3 ± 0.1 μm end radius (Synton-MDP AG, Switzerland). The test consisted of the following steps. I. Pre-scratch topographic scan II. Performing the ramped load scratch with an increase to 100 mN normal load, 2 μm/s velocity, scratch length 150 μm. III. Post-scratch scan. The pre and post scratch topographic scans were performed at low loads 0.02 mN. Each test was repeated at least five times for data statistics. The scratch grooves were investigated by Zeiss optical microscope in interference contrast. Typical scratch morphologies were investigated by SEM (Thermo Scientific Scios 2). Furthermore, the scratch results were interpreted together with cross-sectional XTEM observations of the corresponding deformation and failure mechanisms.

2.4. XTEM studies

The structure of the pristine and irradiated specimens was determined by cross-sectional transmission electron microscope (XTEM). The XTEM measurements were performed in a FEI-Themis Cs-corrected (scanning) transmission electron microscope ((S)TEM), in both HREM (High Resolution Electron Microscope) and STEM (Scanning Transmission Electron Microscope) mode (point resolution is around 0.09 nm in HRTEM mode and 0.16 nm in STEM mode) operated at 200 kV. During TEM imaging, the beam current was typically in the range of 30–220 pA in TEM and HRTEM mode and 20–40 pA in STEM mode, adjusted to minimize beam-induced damage. The energy dispersive X-ray (EDX) mapping was done with a Super-X detector counting four detectors around the TEM sample, the effective collection angle of the system is approximately 0.7 sr (corresponding to ~0–35°). Sample

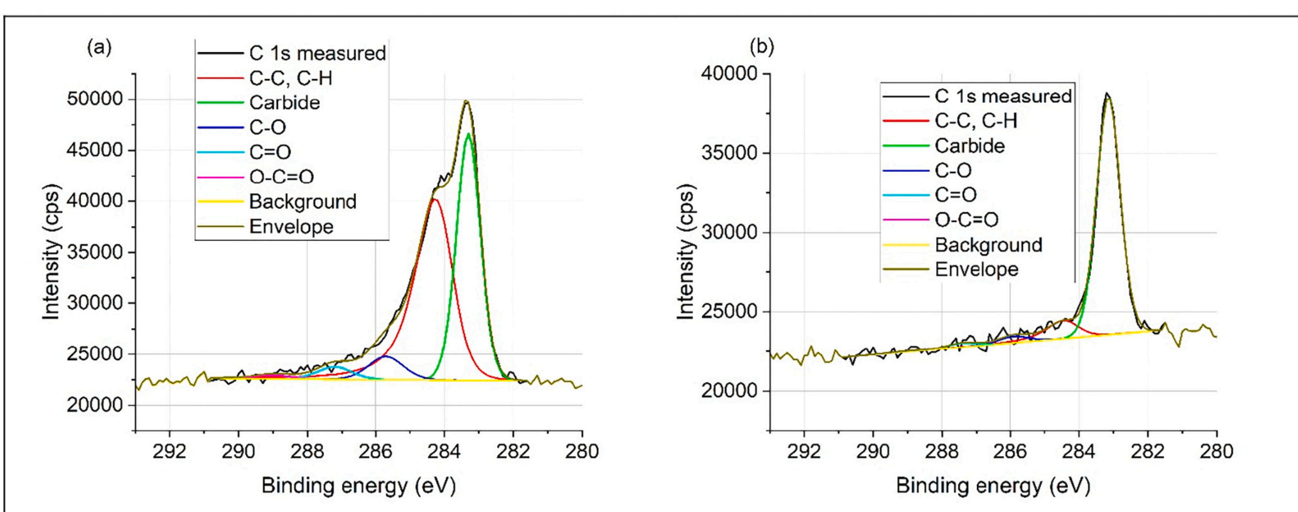

Fig. 1. The decomposed C (1 s) XP spectra of the 102010-Mo 120 keV, 5×10^{15} Xe^+ irradiated sample a. transition region b. carbide region.

preparation for XTEM was made by focused ion beam (FIB) milling. TEM lamellae were prepared with a Thermo Fisher Scientific Scios 2 Dual Beam microscope (Eindhoven, The Netherlands) with an EasyLift™ nanomanipulator. First, a Pt layer was deposited onto the lamella to protect the layer during ion milling in two steps: electron-beam-assisted Pt deposition at 2 keV and 3.2 nA, followed by ion-beam-assisted Pt deposition at 30 keV and 300 pA. Thinning of the lamellae (after digging trenches on both sides) was carried out in three steps using Ga ions: (1) down to a lamella thickness of 150 nm – at 2.5° on both sides with 16 keV per 50 pA; (2) for polishing at 5° on both sides with 5 keV per 48 pA; and (3) for the final polishing at 7° on both sides with 2 keV per 27 pA. Final low-kV cleaning ensured removal of amorphized surface layers and reduction of curtaining.

3. Results

3.1. Structure and composition of nanolayers

The structure of the different starting samples can be seen in the HRTEM images in Fig. 2a and b. The images clearly show that 3 layers are placed on the crystalline Si substrate. It can be seen that all interfaces are sharp. This means that the intensity variations visible at the C/Mo (W) interfaces in the HRTEM images do not exceed the intrinsic roughness of the Si substrate. Furthermore, EDS analysis did not reveal any measurable interdiffusion between the deposited layers beyond the slight apparent blurring attributable to substrate roughness and projection effects. The darker regions correspond to elements with higher atomic numbers, tungsten and molybdenum, respectively. The HAADF images and EDS maps are provided in SI Fig. S1.

Figure c and d shows the HRTEM images of the irradiated samples (120 keV 5 × 10^{15} Xe^+/cm^2 102010-W and 80 keV 102010-Mo). It can be seen that the interfaces became blurred and the Si substrate was strongly amorphized. Interfacial mixing is also confirmed by the EDS line profiles (Supporting Information, Fig. S2). Furthermore, we can see that the thickness of the amorphized Si layer strongly depends on the layer structure. To investigate the origin of this effect, SRIM simulations were performed. Fig. 3a and b show the binary collision events obtained by Monte Carlo simulations together with the corresponding Xe depth distributions (Fig. 3c and d) for the 120 keV 102010-W and 80 keV 102010-Mo irradiations, respectively. Owing to the higher atomic mass of tungsten, the higher irradiation energy results in a Xe projected range (23.1 and 23.6 nm, respectively) comparable to that obtained for the 80 keV 102010-Mo system. However, the longitudinal straggling is considerably larger for the 102010-W system (12.8 nm versus 7.2 nm), leading to a greater fraction of Xe ions penetrating into the Si substrate. Fig. 3e shows the calculated vacancy distribution in the Si substrate, demonstrating a substantially higher vacancy concentration extending to greater depths in the 102010-W system. This finding is in good agreement with the thicker amorphized Si region observed in the XTEM image (Fig. 2c) of this sample.

The XPS depth profiles for the 5 × 10^{15} Xe^+/cm^2 irradiated and non-irradiated samples are provided in Fig. 4. In the non-irradiated (a and b) samples we can see the alternating C and metal layers. Interestingly even in the non-irradiated sample thin carbide layers are shown at the interfaces, this is due to the artifact production of argon sputtering used in XPS depth profiling [24,25]. However, the irradiated samples (c and d)

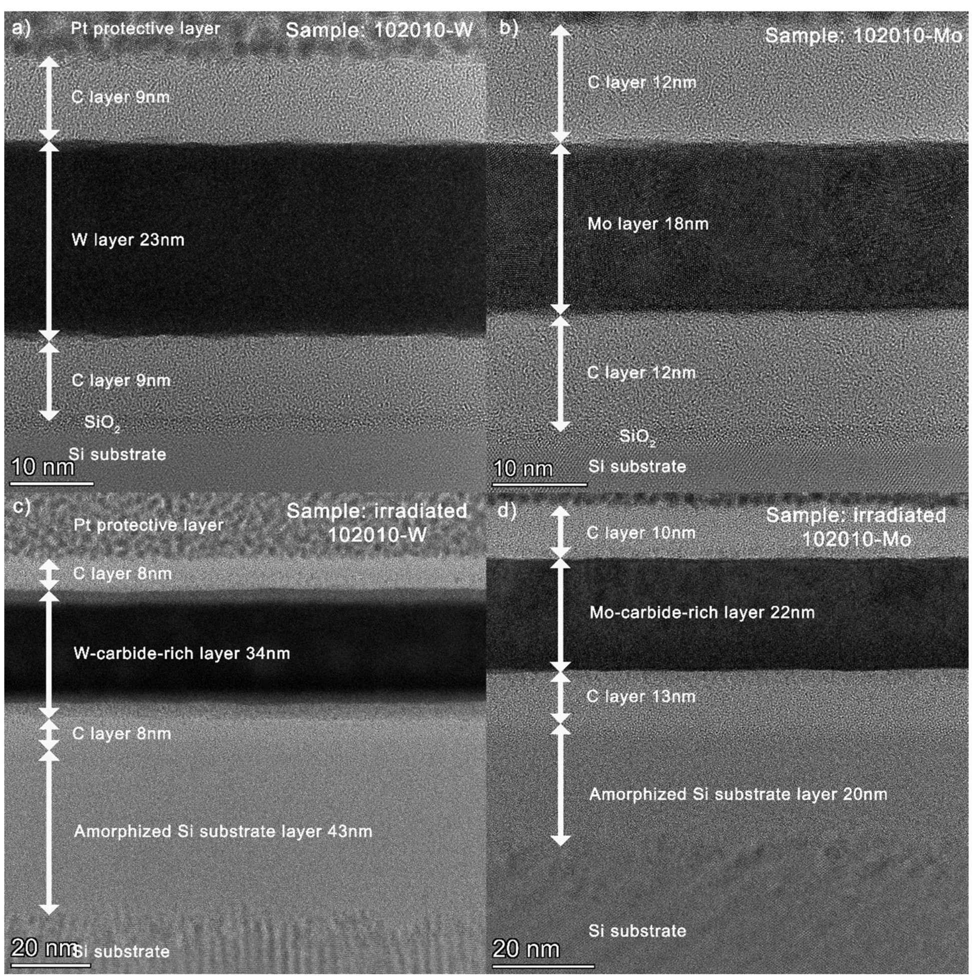

Fig. 2. HRTEM images of the initial layer structures of the 102010-W (a), 102010-Mo (b) samples and after irradiation (c and d 120 and 80 keV Xe^+/cm^2, resp.).

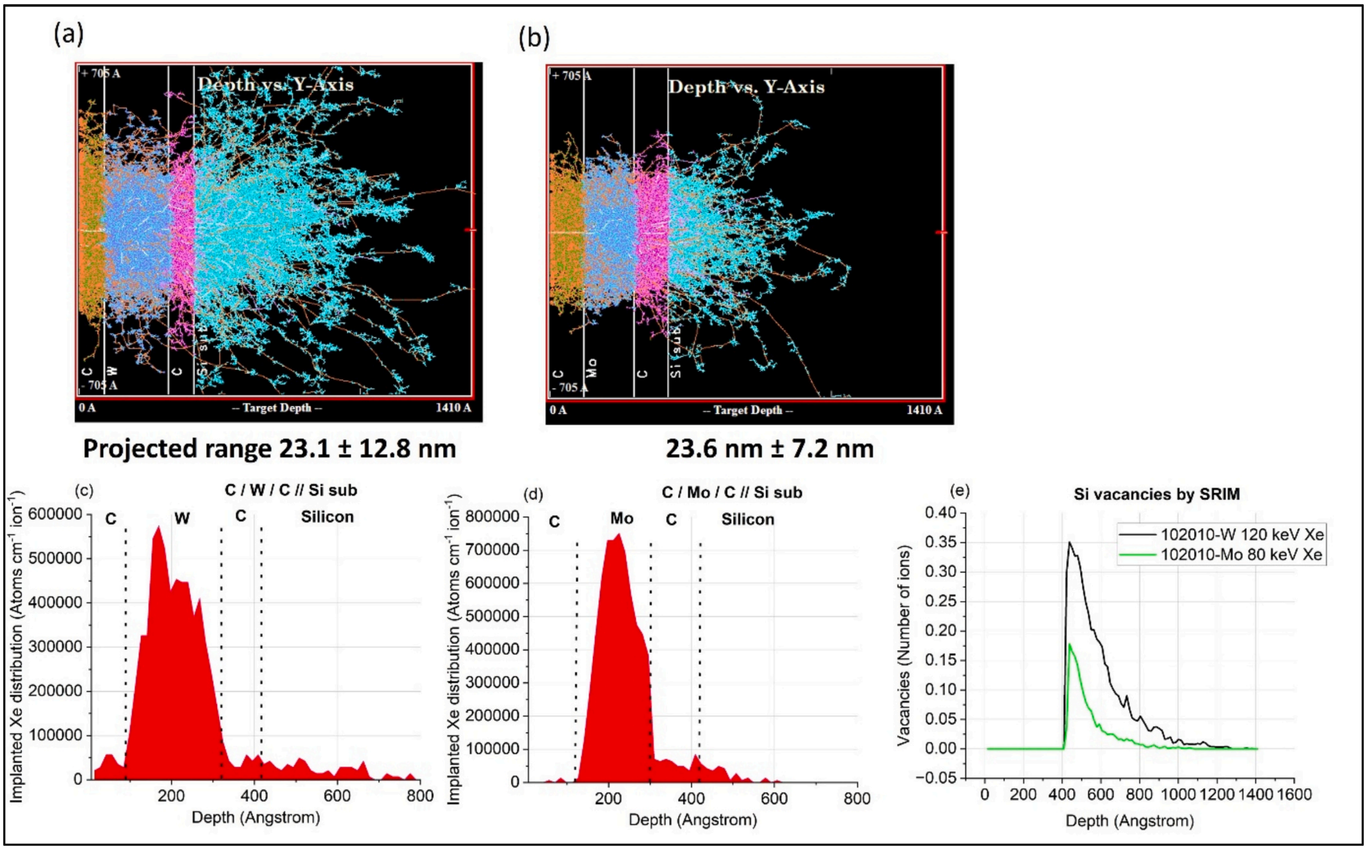

Fig. 3. SRIM simulation results for the projected ranges of a.c 120 keV 102010-W and b.d 80 keV Xe^+ 102010-Mo samples together with the e. simulated vacancies in Si substrate.

show extensive carbide production which is more pronounced for the C/W system. This is due to the higher average atomic number (40 for C/W and 24 for C/Mo) resulting in higher thermal spike mixing. SI Fig.S3 shows that the applied energy not only influences the substrate amorphization but also the carbide production. XPS depth profiles of a 2.5×10^{15} Xe^+/cm^2 102010-W irradiations are shown, the energy varies strongly, Fig.S3a belongs to 40 keV while b to 120 keV irradiations. We can see that in the case of 40 keV only the first interface is affected which is due to the low penetration depth of xenon ions being 13.1 ± 3.4 nm [19]. The Xe distribution obtained from SRIM simulations and the corresponding XTEM image is shown in Fig. S4. The XTEM investigation confirms that no irradiation-induced amorphous layer is formed in the Si substrate under these conditions.

3.2. Morphology and critical loads

The critical loads for coating delamination were determined from the load-displacement curves and microscopic images. Fig. 5 shows scratch distance displacement curves together with the optical images for samples 102010-W and 120 keV 5×10^{15} Xe^+ ion irradiation. Generally, from the scratch test different critical loads can be extracted. L_{c1} is considered when first arc tensile cracks appear which is associated with cohesive failure of the coating. L_{c2} is identified when first chipping or spallation occurs and the substrate is exposed, meaning total film failure. This quantity is related to the adhesive strength of the coating. For our case as the coating thickness was only 40 nm, it was not possible to determine the Lc_1 parameters of the coatings due to the noise of the displacement curves. It is important to note that it was shown previously that L_{c1} is not largely affected by the ion implantation of the substrate. However, differences were observed in the L_{c2} values which is also valid for our case. [26] It can be clearly observed that ion-implanted samples show better adhesive strength, while the reference coating presents a large area of spallation and the defect appears at lower loads. For the reference, coating spallation with substrate exposure starts at 30 μm, while for implanted samples it appears around 70 μm. Analysing the spallation area with optical microscopy images for both reference and implanted sample, more substrate exposure is observed, which corresponds to whiter areas, while in the implanted samples less coating area is lifted exposing the substrate, indicating a better adhesive strength. It can be also seen that the total film removal at L_{c2} is accompanied by extensive deformation of the silicon substrate and (slightly) wavy scratch tracks that are diagnostic of failure in front of the probe. Plastic deformation of the silicon substrate occurs before total film removal, as shown by residual depths greater than the film thickness prior to L_{c2}. After complete coating removal, the scratch response is dominated by deformation of the exposed silicon substrate.

Fig. 6 summarizes the measured critical loads for all irradiation conditions. Ion irradiation improved the adhesion of both multilayer systems; however, the enhancement is considerably more pronounced for the C/W coating. It is also evident that the adhesion improvement strongly depends on the modification of the coating/Si interface. For the 40 keV irradiation of the 102010-W sample (2.5×10^{15} Xe^+/cm^2), the projected range (13.1 ± 3.4 nm according to SRIM [19]) is insufficient to reach the coating/substrate interface. Consequently, the interface remains essentially unaffected (see Fig.S4) and the critical load remains comparable to that of the non-irradiated sample. In contrast, 120 keV irradiation reaches the coating/Si interface, resulting in significant interfacial mixing and extensive amorphization of the Si substrate, as demonstrated by the XTEM observations (Fig. 2c) and supported by the SRIM simulations (Fig. 3). Increasing the Xe fluence from 2.5×10^{15} to 5×10^{15} Xe^+/cm^2 further increases the critical load from approximately 38 mN to 45 mN. This behaviour is consistent with the XPS depth

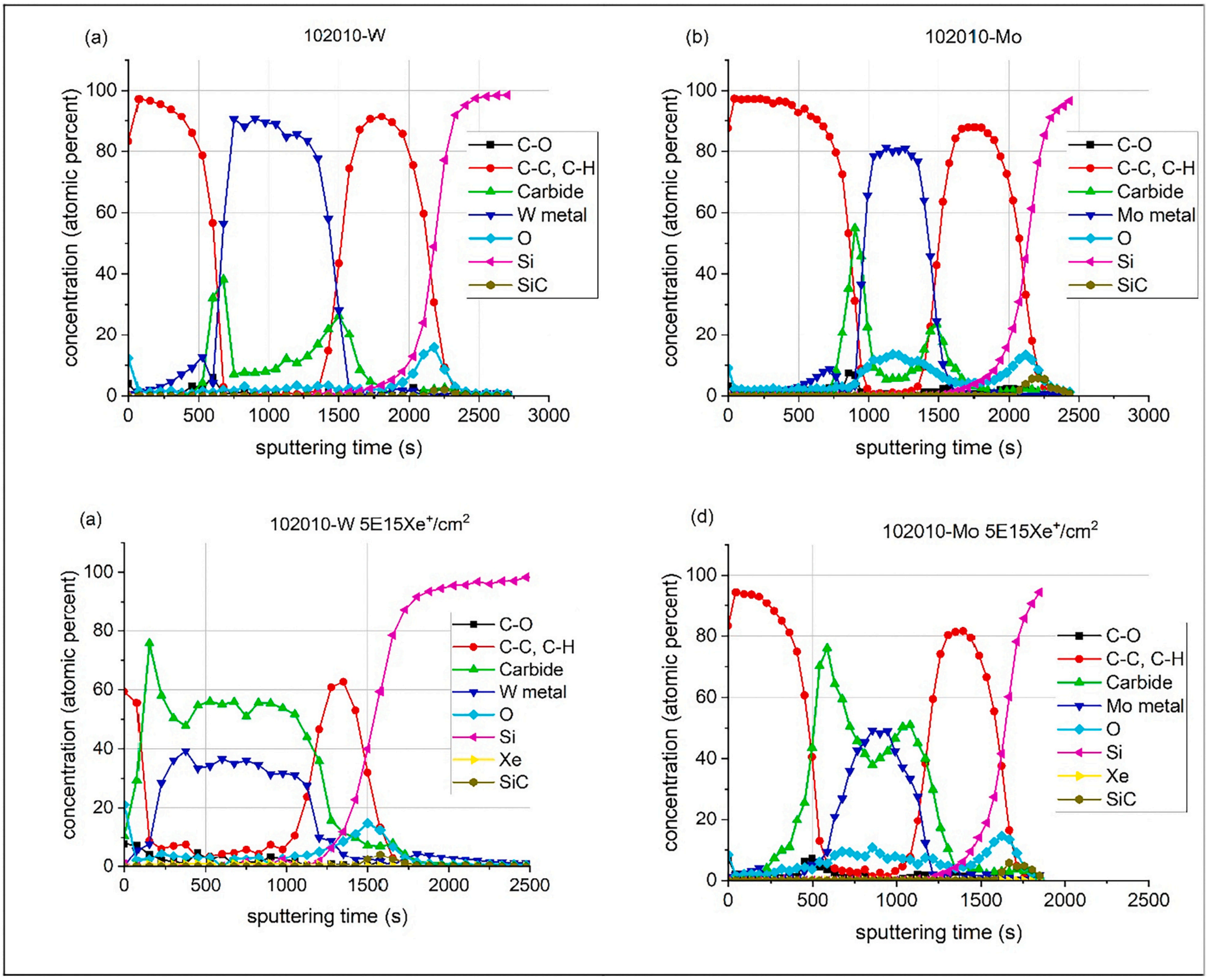

Fig. 4. XPS depth profiles of a. 102010-W b. 102010-Mo and irradiated c. 120 keV 102010-W and d. 80 keV 102010-Mo 5 × 10^{15} Xe^{+}/cm^{2} samples.

profiles, which reveal more pronounced interfacial mixing at the higher fluence (Fig. 4c and Fig. S3b). The adhesion improvement of the C/Mo multilayer is less pronounced than that of the C/W system. This correlates with the thinner amorphized Si region observed by XTEM (Fig. 2d), the lower vacancy production predicted by SRIM (Fig. 3e), and the weaker interfacial mixing revealed by the XPS depth profiles (Fig. 4d). The more extensive mixing observed in the C/W system is consistent with the higher average atomic number of the multilayer, which is expected to enhance irradiation-induced thermal spike mixing. Therefore, the combined effects of deeper substrate amorphization and stronger interface mixing are believed to be responsible for the superior adhesion improvement of the C/W coating.

4. Discussions

The structural changes observed during scratching are discussed based on XTEM analysis. Only a limited number of studies have applied XTEM to investigate deformation and failure mechanisms along scratch tracks in thin film systems. In most cases, analyses are restricted to SEM or FIB-based cross-sections, while TEM investigations typically focus on isolated regions rather than providing a spatially resolved picture along the scratch path. In this context, the present work addresses this gap by performing XTEM analysis at three to four representative locations along the scratch track: at the beginning, in the middle section, and at the end of the scratch.

To examine the subsurface damage induced by nanoscratching, scratch grooves were cross-sectioned perpendicular to the scratch direction. TEM lamellae were primarily prepared perpendicular to both the scratch direction and the sample surface. For each sample, three to four representative locations were selected along the scratch track, as shown in Fig. 7a. Typically, one or two lamellae were prepared from the initial region where plastic deformation begins, one from the region where the substrate deformation becomes evident, and one from the end of the scratch track. Since the normal load increased continuously during scratching, the load corresponding to each selected position was determined from its position along the scratch track. In addition, for selected samples, the microstructure was also examined using TEM lamellae prepared parallel to the scratch direction (Fig. 7b).

4.1. Effects of scratching on single crystal Si

Bright field XTEM images of the sublayer beneath a scratch made by the conical tip on the 102010-W and 102010-Mo samples are shown in Fig. 8 and in Fig. 9.

From the viewpoint of Si crystal deformation, the samples coated with Mo and W layers exhibited similar behaviour. At applied loads of 8 mN and 12 mN, no deformation could be observed in the Si single crystal (Figs. 8a and 9a). At loads of 19, 22, 24, and 27 mN, the XTEM images of the scratches revealed that the Si single crystal became amorphized in a cone-shaped region to a maximum depth of 200–300 nm (Figs. 8b, e, 9b, and e). The amorphization in silicon due to mechanical loading is a well-known phenomenon in the literature. [27] In the 27–55 mN load range

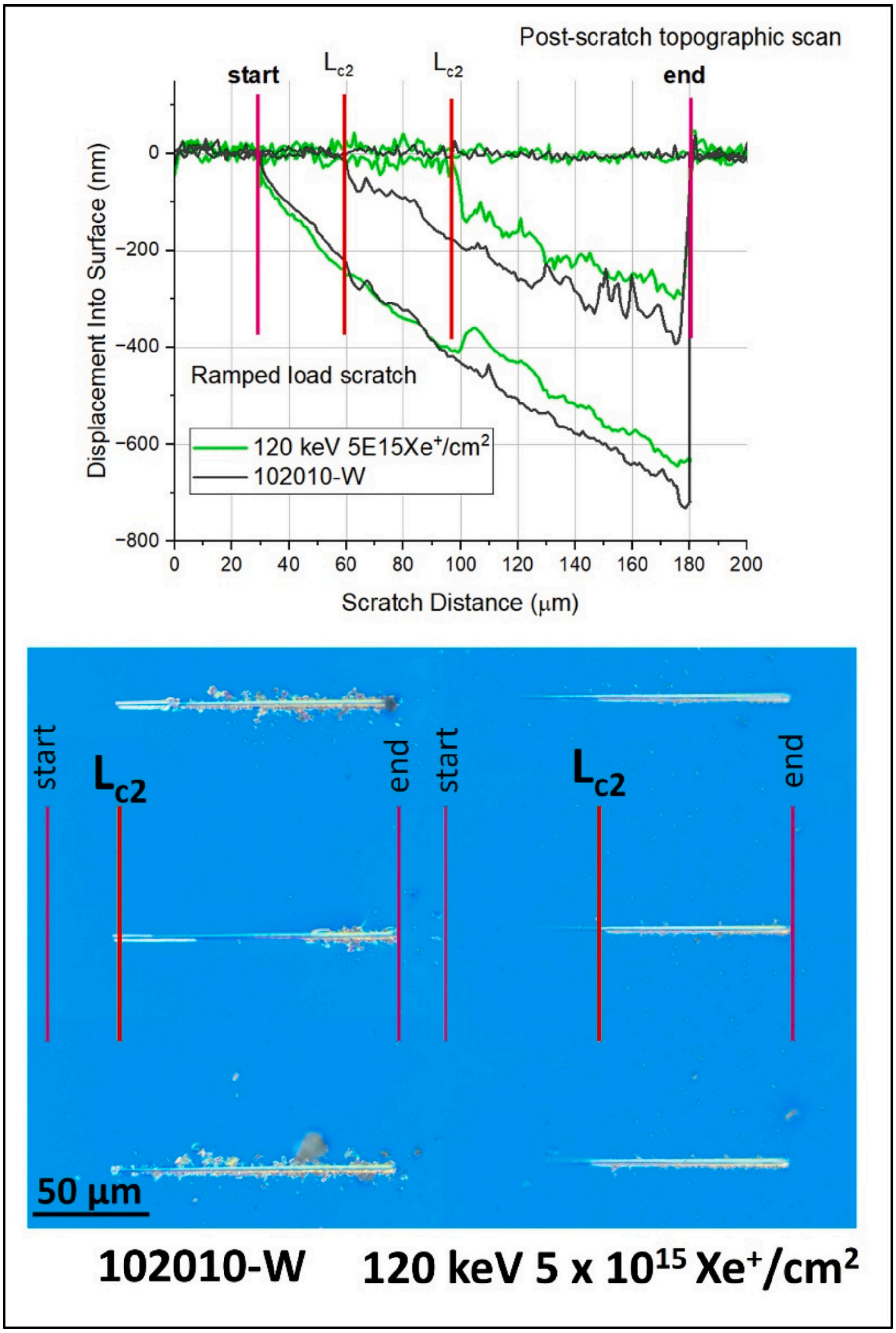

Fig. 5. Scratch distance-displacement curves together with optical microscopy for samples 102010-W and 120 keV 5 × 10^{15} Xe^{+}/cm^{2} irradiation.

significant change occurs in the Si substrate, the amorphous cone-shaped region recrystallization happens and planar defects are appearing under the recrystallized region in parallel with (111) plane. These defects can be attributed to stacking faults found in Si, the contribution of twin lamellas is only minimal, similar to the observations of others. [28–30]

It can be also seen that the TEM samples taken out over 90 mN in the non-irradiated sample cracks are present in the substrate, while these cracks cannot be observed in case of irradiated samples (see Fig. 8d, h, Fig. 9d, h, and Fig. 10 from parallel direction). The displacement curves presented in Fig. 5 for the non-irradiated sample have shown an oscillation in the measured depth at higher penetrations which could be signs of cracks. The absence of cracks in the irradiated samples might be due to the amorphous Si layer due to irradiation. This layer may cause the reduction of the internal stress and act as a lubricant. Sun et al. [31] has shown in ion irradiated Si wafer (110 keV, 1 × 10^{15} to 1 × 10^{17} Ar^{+}/cm^{2},) that the polycrystalline Si layer contributes to the significant increase of critical load of Si because the grains can move against each other under a shearing force and the grain boundaries of the polycrystalline Si grains can stop the propagation of cracks. Tanaka et al. [32] have shown on ductile-cut and brittle-cut surfaces of a-SiC, that microcrack propagation was obstructed at the interface between the amorphous layer and the crystalline base material even under brittle-mode machining and no subsurface damage extended into c-SiC. The results suggested that the damage-free machining of c-SiC is possible by surface modification to an amorphous structure. This advantageous effect of the amorphous layer has been strengthened by molecular dynamics simulation, as well. Chen et al. [33] has shown that the

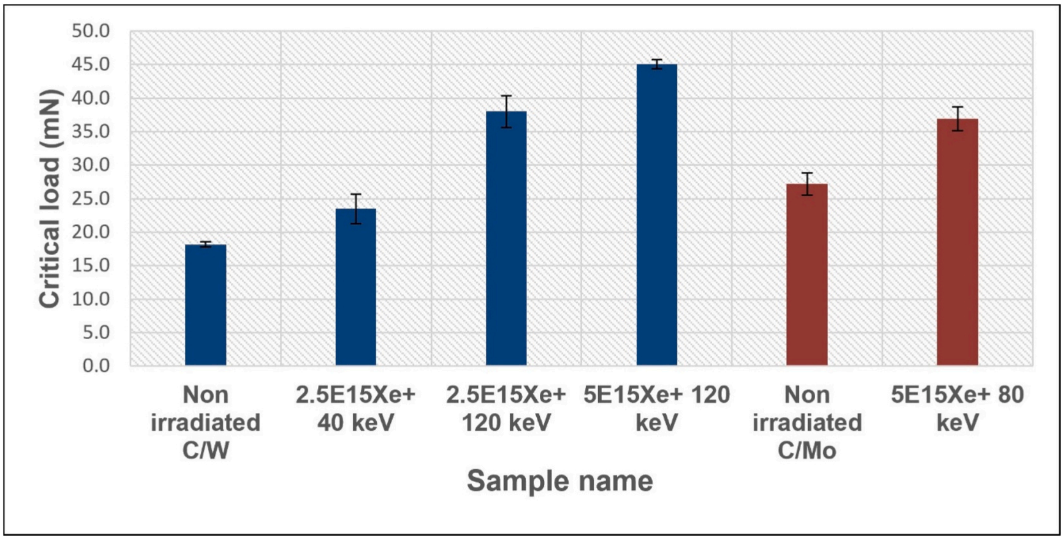

Fig. 6. Critical loads for samples 102010-W and Mo, resp.

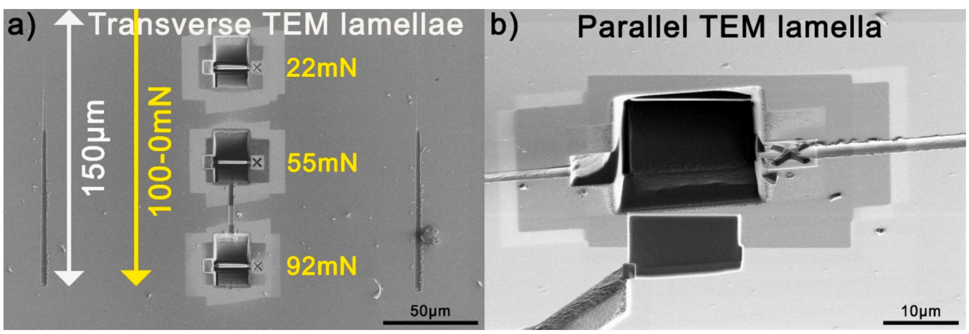

Fig. 7. SEM images showing the scratch tracks and the TEM lamella preparation orientations: a. perpendicular and b. parallel to the scratch direction.

amorphous layer could hinder the crack propagation. The major mechanism is that the strain energy near the crack tip can be fully released through the plastic deformation of amorphous structure, and higher stress is required for the nucleation of secondary crack. This prevents the cleavage fracture in crystalline lattice. The fracture resistance augments with the increase in the amorphous layer thickness. It can be also improved by a double-layer configuration as the separation between the amorphous layers is small enough. In addition, in the crack areas, in the non-irradiated samples, it was observed that the Si orientation could change by a few degrees within 1–2 μm. This change in orientation is visible in Fig. 10a. In the BF TEM image of Fig. 10a, regions corresponding to diffraction are marked with circular rings. The combined diffraction pattern of the electron diffractions delineated by the coloured rings on the BF TEM image is shown on the right side of Fig. 10a, where reflections of different colours form elongated reflections along an arc. The lower SAED image in Fig. 10a was taken from the area bounded by the large white ring (9) in the BF TEM image, where the same arc-shaped elongated reflections can be observed. This indicates an orientation change or grain fragmentation caused by the formation of cracks. Although a contribution from slight lamella bending caused by stress relaxation during FIB specimen preparation cannot be completely excluded, this explanation appears less likely, since arc-shaped reflections were consistently observed only in lamellae containing cracks, whereas crack-free regions exhibited diffraction patterns characteristic of a single crystal. Furthermore, the orientation spread was only detected in a certain depth, supporting its correlation with crack formation rather than with a specimen preparation artifact.

4.2. Effects of scratching on coating layer based on TEM

A significant difference between the irradiated and non-irradiated samples was already observable in the SEM and optical microscopy images. In the non-irradiated samples, the coating detached from the Si surface within the scratches at much lower loads, and the load at which detachment occurred varied from scratch to scratch. In contrast, the irradiated coatings were more stable, and the scratching load at which the coating delaminated from the sample could be defined much more clearly.

In the BF XTEM image of the non-irradiated W sample scratched at a load of 27 mN (Fig. 8c), it can be observed that the coating layer separated from the Si single crystal at a distance of 100–200 nm adjacent to the scratch. This stress-induced delamination also indicates the weak adhesion of the non-irradiated coating. This is further confirmed by the fact that, in the XTEM images of the non-irradiated layers, the edges of the coating are sharply visible in the regions where delamination occurred (Figs. 8c and 9c). In contrast, the irradiated samples exhibited a different failure mode. Rather than abrupt delamination the coating underwent buckling and the buckled coating remained locally connected to the irradiation-modified interface (Figs. 8g and 9g). This change in the failure behaviour is most likely associated with irradiation-induced modification of the coating–substrate interface, including intermixing between carbon and silicon and the formation of a SiC-containing transition region. In addition, irradiation promoted carbide formation within the metallic layers, which may have further strengthened the cohesion between the C and Mo (or W) layers. Together, these structural and chemical modifications account for the

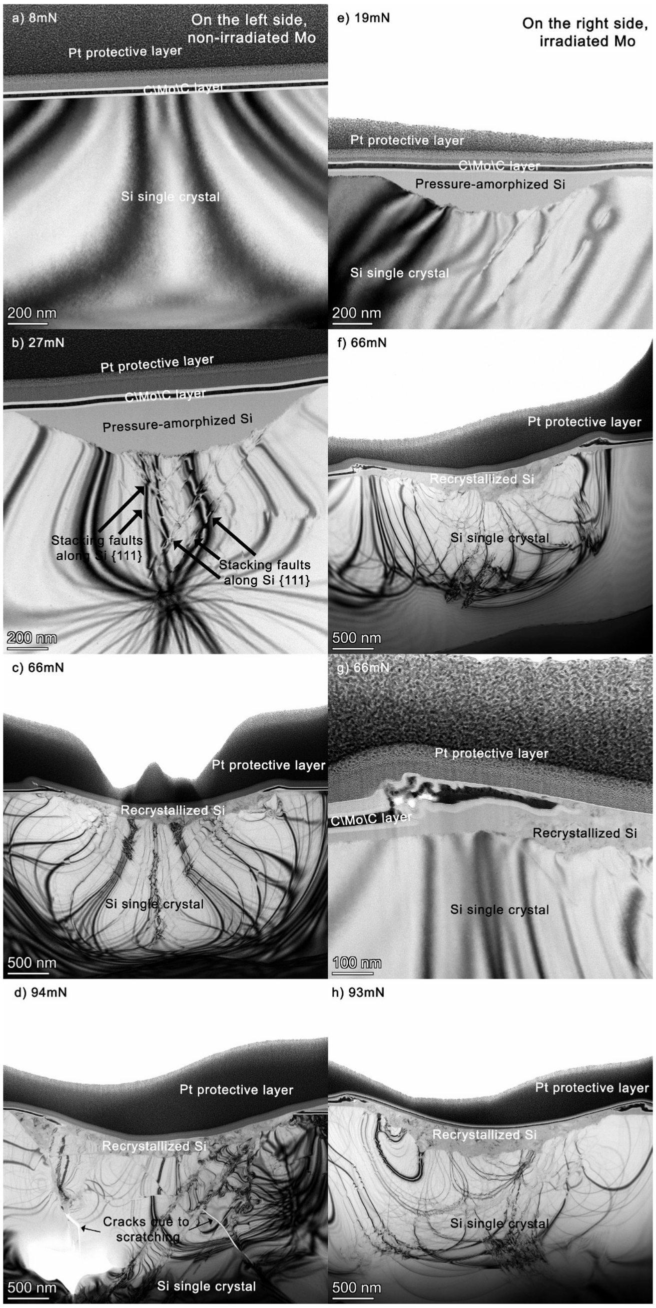

Fig. 8. BF XTEM images of different scratching positions for samples 102010-Mo (a, b, c, d) and 80 keV, 5×10^{15} Xe^{+}/cm^{2} irradiation (e, f, g, h).

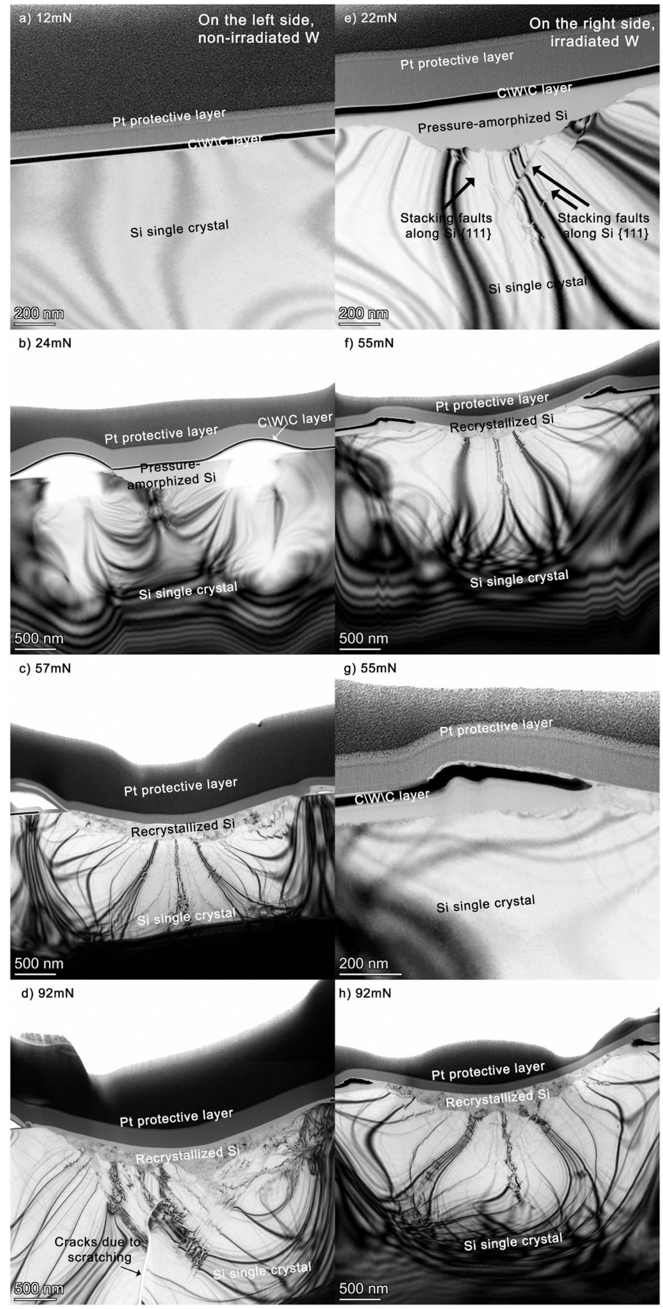

Fig. 9. BF XTEM images of different scratching positions for samples 102010-W (a, b, c, d) and 120 keV, 5×10^{15} Xe^{+}/cm^{2} irradiation (e, f, g, h).

improved adhesion of the irradiated coatings.

Based on the combined XTEM, XPS and SRIM results, the enhanced adhesion of the irradiated coatings appears to originate from two complementary mechanisms. First, irradiation-induced interfacial mixing strengthens the coating/substrate interface allowing the coating to buckle without abrupt delamination. Second, the formation of an amorphous Si layer beneath the coating hinders crack propagation by reducing the brittle response of the crystalline substrate. Both effects are more pronounced for the C/W multilayer, where the XPS depth profiles indicate stronger interfacial mixing and the XTEM observations together with the SRIM simulations reveal a thicker amorphized Si region. These findings consistently explain the larger increase in critical load observed for the C/W system. The importance of modifying the coating–substrate region is further supported by the 40 keV Xe-irradiated 102010-W reference condition. According to SRIM calculations, the projected range at this energy remains within the coating and does not reach the coating–substrate interface. Therefore, this condition provides a comparison where irradiation-induced changes are mainly confined to the coating, suggesting that modification of the coating–substrate region is required for the pronounced adhesion improvement observed after higher-energy irradiation.

Besides interfacial mixing and substrate amorphization, ion irradiation is also known to modify the residual stress state of thin-film systems, which may contribute to the adhesion improvement. For example, an increase in compressive residual stress accompanied by enhanced scratch adhesion after heavy-ion irradiation, which resulted in micrometre-scale modification depths, has been reported for TiN coatings. [9] However, because of the nanoscale thickness of the modified region (approximately 40 nm coating thickness with only a 20–43 nm irradiation-affected Si region) in the present work, direct residual stress

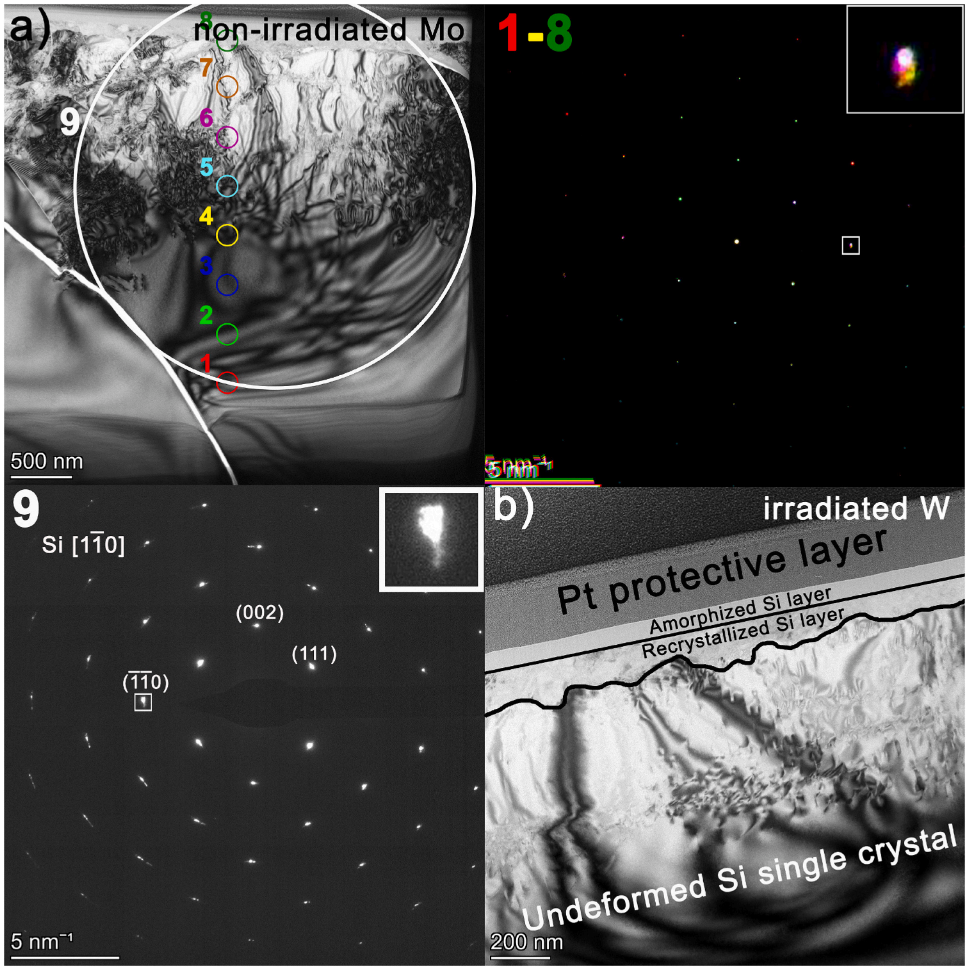

Fig. 10. BF XTEM images of samples cut parallel to the scratching 102010-Mo (a) and 102010-W 80 keV, 5×10^{15} Xe^+/cm^2 irradiation (b) The selected area electron diffraction (SAED) pattern shown next to the BF TEM image (a) is a composite obtained from the regions marked with coloured rings labeled 1–8, while the SAED pattern shown below the BF TEM image (a) was taken from the area bounded by the white ring labeled 9 in the BF TEM image.

determination by conventional techniques such as XRD or substrate-curvature measurements is not straightforward. Therefore, although a contribution of irradiation-induced residual stress cannot be excluded, the present results indicate that interfacial mixing and substrate amorphization are the dominant mechanisms contributing to the observed adhesion improvement.

5. Conclusions

C/W and C/Mo multilayer structures were ion irradiated by xenon ions with various energies and fluences causing carbide formation at the interfaces. The adhesion of the coatings was tested by ramped load scratch test. The critical loads varied for the differently irradiated samples, and it is shown that the ion irradiation improves the adhesion of the coatings. XPS depth profiling has shown that intermixing happened at the interfaces contributing to the improvement of adhesion. Extensive XTEM investigations revealed significant structural changes. Due to ion irradiation a thin amorphous Si layer (20–43 nm) was formed beneath the coating. During scratching, the Si substrate underwent further amorphization at low loads. While at higher loads the amorphized areas of the Si substrate recrystallized. Planar defects and dislocations created by scratching were also observed below the amorphized or recrystallized area. In contrast to the non-irradiated coatings, no substrate cracking was observed in the irradiated samples and the coating buckled instead of abrupt delamination, indicating the enhancement of the mechanical integrity of the coating–substrate system. The combined XPS, XTEM and SRIM results indicate that irradiation-induced interfacial mixing together with the formation of a thin amorphous Si layer suppress crack propagation, strengthen the coating–substrate interface and account for the improved adhesion observed after irradiation.

CRediT authorship contribution statement

A.S. Racz: Writing – review & editing, Writing – original draft, Visualization, Validation, Supervision, Project administration, Methodology, Investigation, Funding acquisition, Formal analysis, Data curation, Conceptualization. **M. Nemeth:** Writing – review & editing, Software, Resources, Methodology. **O. Krafcsik:** Writing – review & editing, Validation, Formal analysis. **U. Kentsch:** Resources, Investigation. **M. Panjan:** Resources, Investigation. **M. Göken:** Resources, Methodology, Supervision. **M. Wurmshuber:** Writing – review & editing, Supervision, Software, Resources, Methodology, Investigation. **Z. Fogarassy:** Writing – review & editing, Writing – original draft, Visualization, Validation, Supervision, Resources, Methodology, Investigation, Data curation.

Declaration of competing interest

The authors declare that they have no known competing financial interests or personal relationships that could have appeared to influence the work reported in this paper.

Acknowledgements

Thanks are given for J. Seltsam for helping with the initial SEM measurements. L. Illes for FIB lamella preparation and EBSD measurements is highly acknowledged. Thanks are given for Dr. P. Panjan for producing the C/W samples. Thanks are given for Dr. M. Menyhard and D. Olasz for discussions. The project was accomplished from DAAD scholarship (AS Racz) and project funding from HUN-REN Centre for Energy Research. The Hungarian authors thank the support of VEKOP-2.3.3-15-2016-00002 of the European Structural and Investment Funds.

Appendix A. Supplementary data

Supplementary data to this article can be found online at https://doi.org/10.1016/j.surfcoat.2026.133868.

Data availability

Data will be made available on request.

References

[1] S. Danaci, L. Protasova, J. Lefevere, L. Bedel, R. Guilet, P. Marty, Efficient CO 2 methanation over Ni/Al 2 O 3 coated structured catalysts, Catal. Today 273 (2016) 234–243, https://doi.org/10.1016/j.cattod.2016.04.019.

[2] Z. Hu, L. Zhang, J. Huang, Z. Feng, Q. Xiong, Z. Ye, Z. Chen, X. Li, Z. Yu, Self-supported nickel-doped molybdenum carbide nanoflower clusters on carbon fiber paper for an efficient hydrogen evolution reaction, Nanoscale 13 (2021) 8264–8274, https://doi.org/10.1039/D1NR00169H.

[3] R. Ali, M. Sebastiani, E. Bemporad, Influence of Ti–TiN multilayer PVD-coatings design on residual stresses and adhesion, Mater. Des. 75 (2015) 47–56, https://doi.org/10.1016/j.matdes.2015.03.007.

[4] F. Ashrafizadeh, Adhesion evaluation of PVD coatings to aluminium substrate, Surf. Coat. Technol. 130 (2000) 186–194, https://doi.org/10.1016/S0257-8972(00)00670-8.

[5] F. Zhu, Z. Chen, K. Liu, W. Liang, Z. Zhang, Deposition of thin tungsten carbide films by dual ion beam sputtering deposition, Vacuum 157 (2018) 45–50, https://doi.org/10.1016/j.vacuum.2018.08.023.

[6] H. Şengül, T.L. Theis, S. Ghosh, Toward Sustainable Nanoproducts, J. Ind. Ecol. 12 (2008) 329–359, https://doi.org/10.1111/j.1530-9290.2008.00046.x.

[7] M. Falsafein, F. Ashrafizadeh, A. Kheirandish, Influence of thickness on adhesion of nanostructured multilayer CrN/CrAlN coatings to stainless steel substrate, Surf. Interfaces 13 (2018) 178–185, https://doi.org/10.1016/j.surfin.2018.09.009.

[8] A. Heidarinejad, F. Ashrafizadeh, Influence of surface texture and coating thickness on adhesion of nickel plated coatings to aluminium substrate, J. Manuf. Process. 120 (2024) 435–448, https://doi.org/10.1016/j.jmapro.2024.04.040.

[9] S. Srivastav, A. Jain, D. Kanjilal, Improvement of adhesion of TiN coatings on stainless steel substrates by high energy heavy ion irradiation, Nucl. Instrum. Methods Phys. Res. B Beam Interact. Mater. Atoms 101 (1995) 400–405, https://doi.org/10.1016/0168-583X(95)00497-1.

[10] Y. Oka, M. Nishijima, K. Hiraga, M. Yatsuzuka, Effect of ion implantation layer on adhesion of DLC film by plasma-based ion implantation and deposition, Surf. Coat. Technol. 201 (2007) 6647–6650, https://doi.org/10.1016/j.surfcoat.2006.09.027.

[11] C.-H. Jung, H.-W. Cho, I.-T. Hwang, J.-H. Choi, Y.-C. Nho, J.-S. Shin, K.-H. Chang, The effects of energetic ion irradiation on metal-to-polymer adhesion, Radiat. Phys. Chem. 81 (2012) 919–922, https://doi.org/10.1016/j.radphyschem.2011.10.012.

[12] N. Nemati, M. Bozorg, O.V. Penkov, D.-G. Shin, A. Sadighzadeh, D.-E. Kim, Functional Multi-Nanolayer Coatings of Amorphous Carbon/Tungsten Carbide with Exceptional Mechanical Durability and Corrosion Resistance, ACS Appl. Mater. Interfaces 9 (2017) 30149–30160, https://doi.org/10.1021/acsami.7b08565.

[13] N. Malone, H. Fiedler, D.R.G. Mitchell, J.V. Kennedy, G.I.N. Waterhouse, P. Gupta, High Turnover Frequency for the Hydrogen Evolution Reaction on Molybdenum Carbide Thin Films Synthesized by Ion Implantation, ACS Appl. Eng. Mater. 1 (2023) 2377–2385, https://doi.org/10.1021/acsaenm.3c00298.

[14] N. Malone, H. Fiedler, D.R.G. Mitchell, J.V. Kennedy, G. Waterhouse, P. Gupta, Grain Boundary-Rich Tungsten Carbide Nanoparticle Films Exhibit High Intrinsic Activity Toward Hydrogen Evolution, ACS Appl. Nano Mater. 7 (2024) 4843–4852, https://doi.org/10.1021/acsanm.3c05497.

[15] A.S. Racz, Z. Kerner, M. Menyhard, Corrosion resistance of tungsten carbide-rich coating layers produced by noble gas ion mixing, Appl. Surf. Sci. 605 (2022) 154662, https://doi.org/10.1016/j.apsusc.2022.154662.

[16] A.S. Racz, P. Kun, Z. Kerner, Z. Fogarassy, M. Menyhard, Tungsten Carbide Nanolayer Formation by Ion Beam Mixing with Argon and Xenon Ions for Applications as Protective Coatings, ACS Appl. Nano Mater. 6 (2023) 3816–3824, https://doi.org/10.1021/acsanm.2c05505.

[17] A.S. Racz, Z. Fogarassy, U. Kentsch, P. Panjan, M. Menyhard, Design and production of tungsten-carbide rich coating layers, Appl. Surf. Sci. 586 (2022) 152818, https://doi.org/10.1016/j.apsusc.2022.152818.

[18] A.S. Racz, Z. Fogarassy, P. Panjan, M. Menyhard, Evaluation of AES depth profiles with serious artefacts in C/W multilayers, Appl. Surf. Sci. 582 (2022) 152385, https://doi.org/10.1016/j.apsusc.2021.152385.

[19] SRIM Stopping and range of ions in matter by Ziegler, J. F. version SRIM, 2013 Software freely available www.srim.org., (n.d.).

[20] D. Briggs, M.P. Seah (Eds.), Practical surface analysis: by auger and x-ray photoelectron spectroscopy, Wiley, Chichester ; New York, 1983.

[21] Copyright © 2005 Casa Software Ltd, (n.d.). http://www.casaxps.com/ (accessed July 18, 2023).

[22] R. Blume, D. Rosenthal, J. Tessonnier, H. Li, A. Knop-Gericke, R. Schlögl, Characterizing graphitic carbon with X-ray photoelectron spectroscopy: a step-by-step approach, ChemCatChem 7 (2015) 2871–2881, https://doi.org/10.1002/cctc.201500344.

[23] B.D. Beake, A.J. Harris, T.W. Liskiewicz, Review of recent progress in nanoscratch testing, Tribol. - Mater. Surf. Interfaces 7 (2013) 87–96, https://doi.org/10.1179/1751584X13Y.0000000037.

[24] A.S. Racz, M. Menyhard, XPS depth profiling of nano-layers by a novel trial-and-error evaluation procedure, Sci. Rep. 14 (2024) 18497, https://doi.org/10.1038/s41598-024-69495-0.

[25] A.S. Racz, M. Menyhard, Evaluation methods for XPS depth profiling; A review, Appl. Surf. Sci. Adv. 30 (2025) 100872, https://doi.org/10.1016/j.apsadv.2025.100872.

[26] L. Ortiz-Membrado, S. García-González, J. Orrit-Prat, R. Bonet, J. Caro, J.F. De Ara, E. Almandoz, L. Llanes, E. Jiménez-Piqué, Improved adhesion of cathodic arc PVD AlCrSiN coating on ion-implanted WC-Co substrates, Int. J. Refract. Met. Hard Mater. 113 (2023) 106187, https://doi.org/10.1016/j.ijrmhm.2023.106187.

[27] Y.-C. Wang, W. Zhang, L.-Y. Wang, Z. Zhuang, E. Ma, J. Li, Z.-W. Shan, In situ TEM study of deformation-induced crystalline-to-amorphous transition in silicon, NPG Asia Mater. 8 (2016) e291, https://doi.org/10.1038/am.2016.92.

[28] M.Y. Chou, M.L. Cohen, S.G. Louie, Theoretical study of stacking faults in silicon, Phys. Rev. B 32 (1985) 7979–7987, https://doi.org/10.1103/PhysRevB.32.7979.

[29] M.D. Stiles, D.R. Hamann, Electron transmission through silicon stacking faults, Phys. Rev. B 41 (1990) 5280–5282, https://doi.org/10.1103/PhysRevB.41.5280.

[30] J.A. Araujo, G.M. Araujo, R.M. Souza, A.P. Tschiptschin, Effect of periodicity on hardness and scratch resistance of CrN/NbN nanoscale multilayer coating deposited by cathodic arc technique, Wear 330–331 (2015) 469–477, https://doi.org/10.1016/j.wear.2015.01.051.

[31] R. Sun, T. Xu, Q. Xue, Effect of Ar+ ion implantation on the nano-mechanical properties and microstructure of single crystal silicon, Appl. Surf. Sci. 249 (2005) 386–392, https://doi.org/10.1016/j.apsusc.2004.12.015.

[32] H. Tanaka, S. Shimada, Damage-free machining of monocrystalline silicon carbide, CIRP Ann. 62 (2013) 55–58, https://doi.org/10.1016/j.cirp.2013.03.098.

[33] R. Chen, J. Wang, F. Fang, X. Zhang, Influence of buried modified layer on crack propagation and diamond turning of silicon, Precis. Eng. 55 (2019) 426–432, https://doi.org/10.1016/j.precisioneng.2018.10.011.